Available online at www.sciencedirect.com
ScienceDirect
Trans. Nonferrous Met. Soc. China 26(2016) 1472−1481
Transactions of Nonferrous Metals Society of China
www.tnmsc.cn

Influence of thermomechanical treatments on localized corrosion susceptibility and propagation mechanism of AA2099 Al−Li alloy

Yan-long MA[1], Xiao-rong ZHOU[2], Xiao-min MENG[1], Wei-jiu HUANG[1], Yi LIAO[3], Xiao-li CHEN[1], Ya-nan YI[1], Xin-xin ZHANG[2], G. E. THOMPSON[2]

1. College of Materials Science and Engineering, Chongqing University of Technology, Chongqing 400054, China;
2. Corrosion and Protection Centre, School of Materials, University of Manchester, Manchester M13 9PL, UK;
3. Chongqing University of Education, Chongqing 400067, China

Received 25 June 2015; accepted 10 November 2015

Abstract: In order to manifest the influence of specific microstructural component on the development of severe localized corrosion in an AA2099 aluminum−lithium alloy, the corrosion behavior of the alloy subjected to solution heat treatment, cold working and artificial ageing was investigated. Immersion testing and potentiodynamic polarization were employed to introduce localized corrosion; scanning electron microscopy and transmission electron microscopy were used to characterize the alloy microstructure and corrosion morphology. It was found that the susceptibility of the alloy to severe localized corrosion was sensitive to thermomechanical treatments. Additionally, the state of alloying elements influenced the mechanism of localized corrosion propagation. Specifically, the alloy in T8 conditions showed higher susceptibility to severe localized corrosion than that in other conditions. During potentiodynamic polarization, the alloy in solution heat-treated and T3 conditions displayed crystallographic corrosion morphology while the alloy in T6 and T8 conditions exhibited selective attack of grain interiors and grain boundaries in local regions.

Key words: aluminum−lithium alloy; corrosion; pitting; polarization; heat treatment

1 Introduction

High performance aluminum−lithium (Al−Li) alloys have attracted much interest due to their relatively low density, high specific strength and stiffness, as well as similar or superior damage tolerance [1−3]. It is found that, with every 1% addition of Li to aluminum, the density of the resultant aluminum alloy decreases by 3% and the elasticity modulus increases by 6% [4]. To date, the development of Al−Li alloys has experienced three generations [5]. The 1st and 2nd generation alloys did not receive wide application mainly due to mechanical anisotropy [6,7] and high corrosion susceptibility [8−15]. The 3rd generation alloys, with increased Cu/Li mass ratio and the addition of other minor elements such as Ag and Zn [16], have overcome the main drawback of the previous alloys and have been increasingly used in aerospace industry. A representative 3rd generation Al−Li alloy is AA2099 alloy, which has been used for floor beams, fuselage and wing stringers of aircrafts.

As a high strength aluminum alloy, AA2099 alloy is not immune to localized corrosion [8−15] in corrosive environment due to its deliberately developed heterogeneous microstructure for achieving desirable mechanical properties. BUCHHEIT et al [9−11] studied the corrosion behavior of AF/C 458 alloy and found that pitting corrosion in the alloy was intimately related to constituent particles and the particles might promote grain/subgrain boundary attack if they appeared in grain/subgrain boundary regions, and that T_1 (Al_2CuLi) phase was the major cause of grain/subgrain boundary attack. LI et al [15] studied the corrosion behavior of bulk T_1 phase, suggesting that T_1 phase was anodic to the alloy matrix in early stages of corrosion and subsequently became cathodic as the consequence of preferential dissolution of aluminum and lithium from T_1 phase. The role of T_1 phase in localized corrosion of

Foundation item: Projects (51301214, 51441002) supported by the National Natural Science Foundation of China; Project (cstc2013jcyjA50017) supported by Fundamental and Cutting-edge Research Plan of Chongqing, China; Project supported by EPSRC LATEST2 Program, UK; Project supported by Scientific Research Foundation for the Returned Overseas Chinese Scholars, State Education Ministry
Corresponding author: Wei-jiu HUANG; Tel: +86-23-62563089; E-mail: huangweijiu@cqut.edu.cn
DOI: 10.1016/S1003-6326(16)64252-8

other Al−Cu−Li alloys was investigated by comparing the corrosion behavior of the alloys subjected to different heat treatments [17,18]. Recent work on corrosion behavior of AA2099-T8 alloy has suggested that the alloy was susceptible to severe localized corrosion (SLC) in chloride-containing environment [19−21]. It was suggested that two factors, i.e., dislocation density (or stored energy) within grains and preferential precipitation of T_1 phase at crystallographic imperfections, played a critical role in developing SLC in the alloy. Nevertheless, it is difficult to differentiate the effect of the two factors during the process of a localized corrosion event because the two factors often coexist in local regions in the alloy in T8 temper (i.e. cold working plus artificial aging). The purpose of the work is to manifest the influence of specific microstructural component on the development of SLC, which is achieved by comparing the corrosion behavior of an AA2099 aluminum−lithium alloy subjected to solution heat treatment, cold working and artificial aging. It is suggested that the combined effect of cold working and artificial aging is responsible for the development of SLC in the alloy of T8 condition. The suggestion is further supported by the revelation of characteristic corrosion feature (i.e., narrow and parallel corrosion volumes), with its geometry identical to the slip band.

2 Experimental

The received material is an extruded T-shaped beam of AA2099-T8 aluminum alloy. The chemical composition of the alloy is given below: 1.62% Li, 2.83% Cu, 0.72% Zn, 0.30% Mg, 0.29% Mn, 0.04% Fe, 0.06% K, 985×10^{-6} Zr, 180×10^{-6} Si, 1.5×10^{-6} Ag, Al balance. The as-received alloy was annealed at 540 °C for 5 h in a box heat-treatment furnace (CTJZH FURNACE 1000, ±1 °C) and then immediately quenched in icy water, hereafter referred to as solution heat treated (SHT) specimen. Rectangular specimens of 120 mm × 30 mm × 10 mm were machined from the SHT coupon and stretched, in the extrusion direction, to 3% elongation at ambient temperature, hereafter referred to as T3 specimen. Finally, selected SHT and T3 specimens were further aged at 150 °C for 24 h and the resultant specimens were hereafter referred to as T6 and T8 specimens, respectively.

Specimens of 30 mm × 20 mm × 5 mm were machined from alloy coupons of different tempers and then successively ground with 400, 600, 800, 1000 and 2500 grit silicon carbide abrasive papers. Following mechanical polishing, the specimens were degreased in acetone, rinsed in deionized water and dried in a stream of cold air. For metallographic observation, the polished specimens were immersed in a mixed solution (1 mL HF + 2.5 mL HNO_3 + 1.5 mL HCl + 95 mL H_2O) for 2 min, and then desmutted in 30% HNO_3 solution for 30 s before rinsing in deionized water and drying in a stream of cold air. Microhardness measurement was performed on a HVS−1000 microhardness tester, with a load of 100 g and an applied time of 15 s. The final microhardness value of each specimen was determined by averaging 10 measurements.

Potentiodynamic polarization was performed in a 3.5% NaCl solution at ambient temperature, with the specimen, a saturated calomel electrode (SCE) and a platinum plate as working electrode, reference electrode and auxiliary electrode, respectively. The polarization was started from −100 mV to either 200 or 500 mV with respect to the open circuit potential (OCP) at a scanning rate of 0.5 mV/s. Before polarization, the specimen was immersed in the solution for 30 min to reach a relatively stable OCP. In order to reveal the corrosion morphology of the alloy after polarization, the polarized specimens were desmutted in 30% HNO_3 solution for 30 s to remove corrosion product before rinsing in deionized water and drying in a cold air stream. For comparison, potentiodynamic polarization was also performed on electropolished (in a mixed solution of 20% (volume fraction) perchloric acid + 80% (volume fraction) ethanol, at 20 V and 5 °C for 5 min) pure aluminum (99.99% Al) under the selected conditions. The tested specimens were desmutted and cleaned as described to remove corrosion product from the alloy surface. Immersion testing was carried out in an aqueous 3.5% NaCl solution at ambient temperature (~25 °C) for 300 min. The surfaces of the specimens were monitored using an in situ optical system during immersion. All the chemical/electrochemical tests were repeated once to confirm the repeatability.

The alloy microstructure and corrosion morphology were examined on Zeiss Axio Imager A 10 optical microscope and JEOL-JSM−6460LV scanning electron microscope (SEM). For transmission electron microscopy (TEM), electron transparent foils were produced by twin-jet electropolishing the alloy in a Tenupol−3 instrument at 20 V in a mixed solution of 30% (volume fraction) nitric acid and 70% (volume fraction) methanol at about −30 °C. TEM images were taken on a Joel 2000 FXII transmission electron microscope, operated at an accelerating voltage of 120 kV.

3 Results

3.1 Microstructure

Figure 1(a) shows a backscatter electron micrograph of the as-received AA2099-T8 alloy after etching, revealing elongated grains. The grain boundaries were

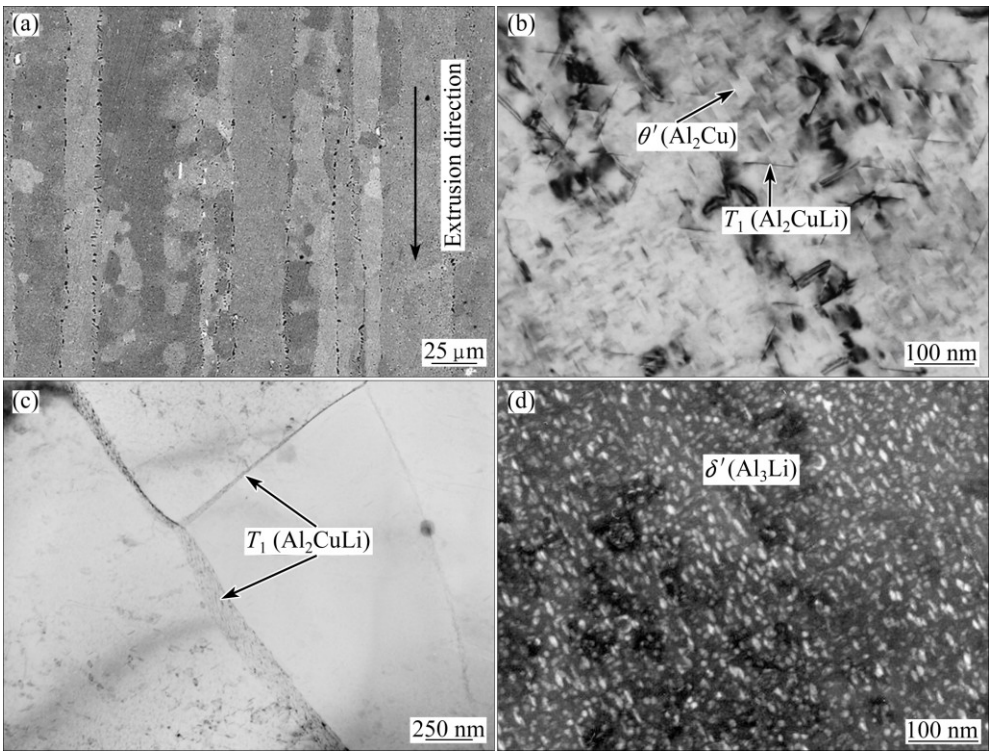

Fig. 1 SEM image of AA2099-T8 alloy after caustic etching, revealing grain structure (a), bright field TEM image showing T_1 (Al_2CuLi) and θ' (Al_2Cu) phase in alloy matrix (b), bright field TEM image showing T_1 (Al_2CuLi) phase at grain boundaries (c), and dark field TEM image obtained by choosing (100) diffraction spots of δ' (Al_3Li) phase, showing distribution of δ' (Al_3Li) phase (d)

surrounded by small cavities that were generated as a consequence of preferential etching of intermetallic particles [5]. The small grains within the elongated grains, identified by channeling contrast associated with grain orientation, were subgrains [5]. Figure 1(b) shows strengthening precipitates of T_1 (Al_2CuLi) and θ' (Al_2Cu) phases in the AA2099-T8 alloy matrix. Figure 1(c) shows the distribution of the T_1 phase at grain boundaries. Dark field TEM image of the alloy (Fig. 1(d)), using the (100) diffraction spots of δ' (Al_3Li) phase, shows the distribution of the δ' phase in the alloy matrix.

Microhardness measurement confirmed the tempers of the alloy after the selected heat treatments, as shown in Fig. 2. The SHT specimen had the lowest microhardness of HV 128.5. When the SHT specimen was stretched to 3% elongation (T3), the microhardness increased to HV 146.3 due to work hardening and subsequent natural aging. Artificial aging treatments on the SHT and T3 specimens at 150 °C for 24 h resulted in increase of microhardness to HV 155.5 for the T6 specimen and to HV 188.1 for the T8 specimen, respectively. The hardness of the T8 specimen is comparable with that of the commercial AA2099-T83 alloy (HV 178.1). The microhardness of the T8 specimen is HV 32.6 higher than that of the T6 specimen, suggesting that cold working significantly accelerated artificial ageing. It is noted that the T6 specimen is

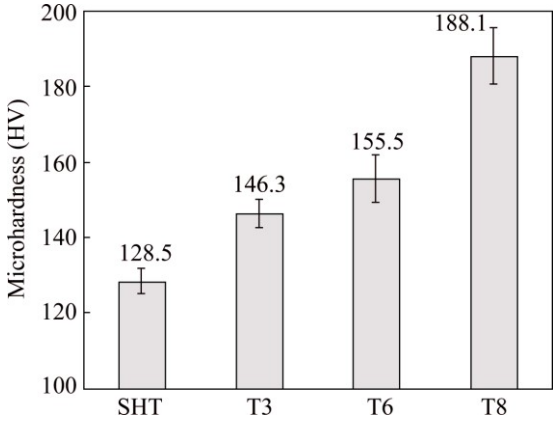

Fig. 2 Measured microhardness of alloy in solution heat treated (SHT), T3, T6 and T8 conditions

under-aged in the selected conditions and, therefore, the T6 condition in the present work is only used for comparing with the T8 condition and should not be regarded as commercial T6 alloy.

3.2 Potentiodynamic polarization

Figure 3(a) shows the OCPs of the alloys recorded during immersion, revealing a relatively stable OCP for the SHT, T3, T6 and T8 specimens after immersion for 30 min. Figure 3(b) shows potentiodynamic polarization curves of the SHT, T3, T6 and T8 specimens recorded during polarization from −0.1 to 0.5 V (OCP). No evident passivation was revealed on the curves,

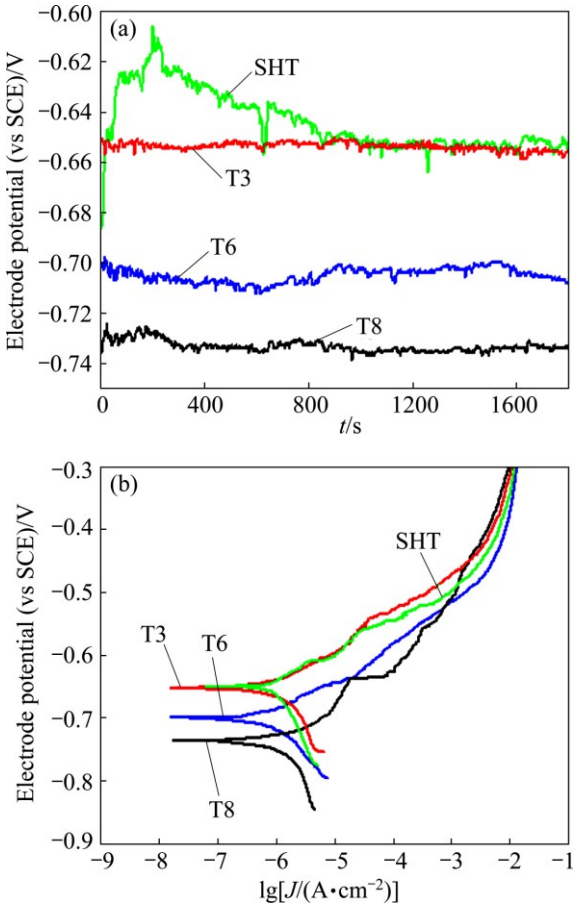

Fig. 3 Open circuit potentials (a) and potentiodynamic polarization curves of alloy in 3.5% NaCl solution under SHT, T3, T6 and T8 conditions (b)

suggesting that the alloy remained active during the anodic polarization process. The current densities were comparable with the same over-potential while the corrosion potentials of the alloy in different tempers were evidently different. The T8 specimen had the most negative corrosion potential, −736.6 mV, suggesting that the specimen was thermodynamically more susceptible to corrosion than other specimens under the selected conditions. The SHT specimen had the most positive corrosion potential, −648.3 mV, representing relatively high corrosion resistance under the selected conditions. The corrosion potential of the T6 specimen (−700.0 mV) was more positive than that of the T8 specimen, but was more negative than those of the T3 (−653.0 mV) and SHT specimens, indicating that artificial aging generally shifted the corrosion potential of the alloy in negative direction, no matter there was cold working or not. The corrosion potential of the T3 specimen was only slightly more negative than that of the SHT specimen, suggesting that cold working alone, thermodynamically, had a very limited effect on the corrosion resistance of the alloy.

In order to correlate the electrochemical process occurring during potentiodynamic polarization to the microstructure of the alloy and to the mechanism of corrosion, the corrosion morphology of the specimens after polarization was examined. Figure 4 shows SEM images of the SHT, T3, T6 and T8 specimens after potentiodynamic polarization from −100 to 500 mV (OCP), revealing localized corrosion sites (the bright regions) on the specimens. It was noticed that the distribution of corrosion sites between the alloys of different tempers was different. The surface area fraction of corrosion sites on the T8 specimen was smaller compared with other specimens. Further, the corrosion sites were elongated in the extrusion/stretching direction for the T6 and T8 specimens, distinct from the irregular shape and random distribution of the corrosion sites on the SHT and T3 specimens.

Figure 5 shows SEM images of the alloy in T8 condition after potentiodynamic polarization, at increased magnification. It is clearly revealed in Fig. 5(a) that SLC occurred in the alloy. Focusing on the framed regions *A* and *B* in Figs. 5(a)−(c) reveal that corrosion propagated preferentially in the extrusion/stretching direction. Figure 5(d) shows the SEM image taken from the frame region *C* in Fig. 5(c), revealing polishing marks and selectively attacked intermetallics (indicated by the arrows), suggesting that the alloy matrix away from localized corrosion sites was only mildly attacked. Typical corrosion pits on the T6 specimen after potentiodynamic polarization are shown in Fig. 6, revealing, again, preferential propagation of corrosion in the extrusion/stretching direction, although the surface area of the pits on the T6 specimen seemed to be larger compared with that of the pits on the T8 specimen.

Compared with the T8 and T6 specimens, the SHT specimen exhibited different corrosion morphologies (Figs. 7(a) and (b)). It is evident in Fig. 7(a) that the propagation of localized corrosion was independent of the extrusion/stretching direction. Further, within the localized corrosion region, the corrosion of the alloy was more uniform compared with the T6 and T8 specimens. Figure 7(b) displays the framed region in Fig. 7(a) at increased magnification, exhibiting facets in the corroded region. Such corrosion morphology indicates crystallographic corrosion, with the facets corresponding to $\{100\}_{Al}$ crystalline planes [22−25]. The corrosion morphology of the T3 specimen (Figs. 7(c) and (d)) was comparable to that of the SHT specimen, although the facets of crystallographic corrosion were less well defined in the T3 specimen compared with the SHT specimen.

For comparison, a cold-rolled, high purity aluminum sheet was polarized under the same conditions as described above and examined using SEM. At low magnification, the corrosion morphology of the pure aluminum sheet (Fig. 8(a)) was similar to those of the

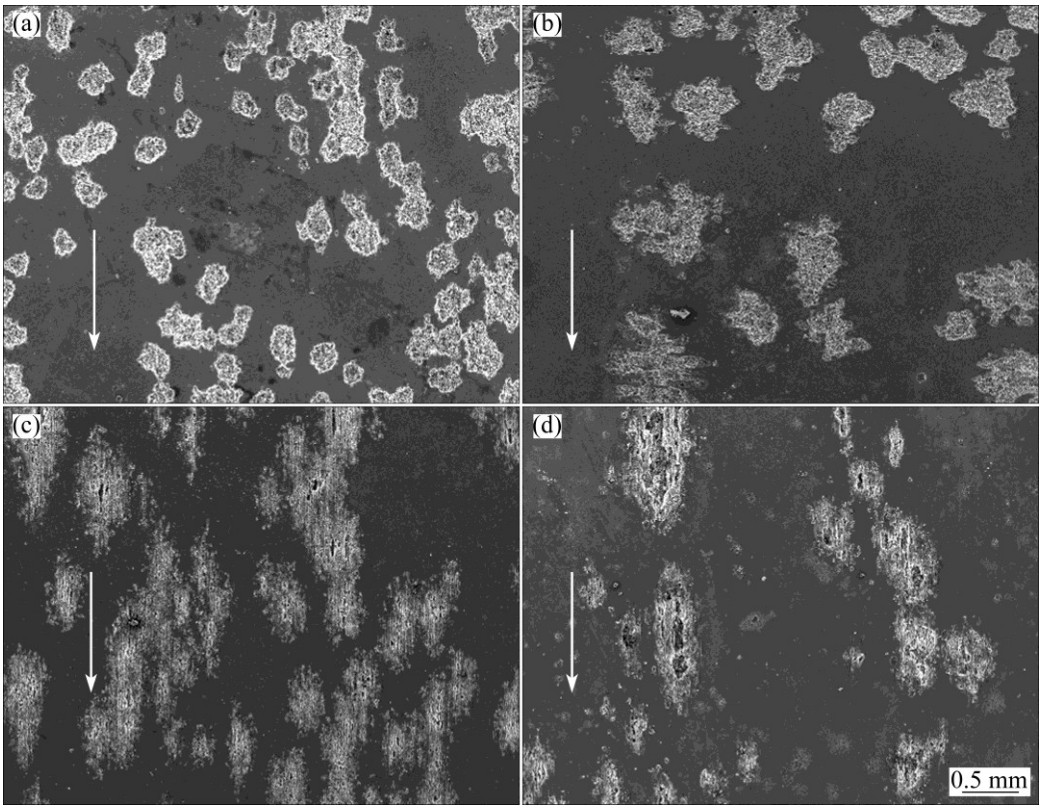

Fig. 4 SEM images of alloy after potentiodynamic polarization from −100 to 500 mV (OCP): (a) SHT; (b) T3; (c) T6; (d) T8 (Arrow in each micrograph indicates extrusion/ stretching direction)

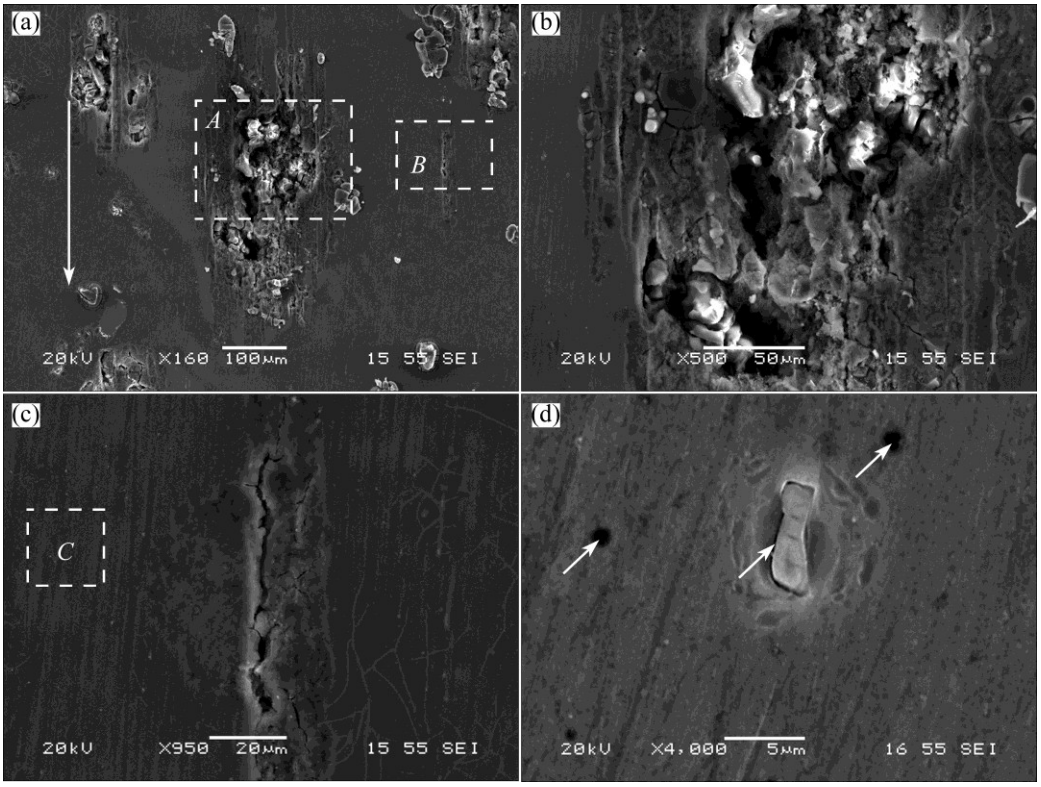

Fig. 5 SEM images of alloy in T8 condition after potentiodynamic polarization from −100 to 500 mV (OCP) (Arrow in (a) indicates extrusion/ stretching direction)

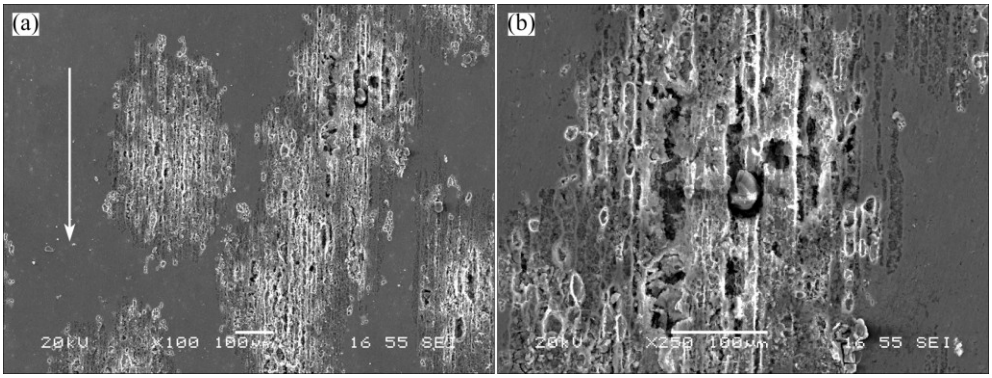

Fig. 6 SEM images of alloy in T6 condition after potentiodynamic polarization from −100 mV (OCP) to 500 mV (OCP): (a) Low magnification; (b) High magnification (Arrow in (a) indicates extrusion/stretching direction)

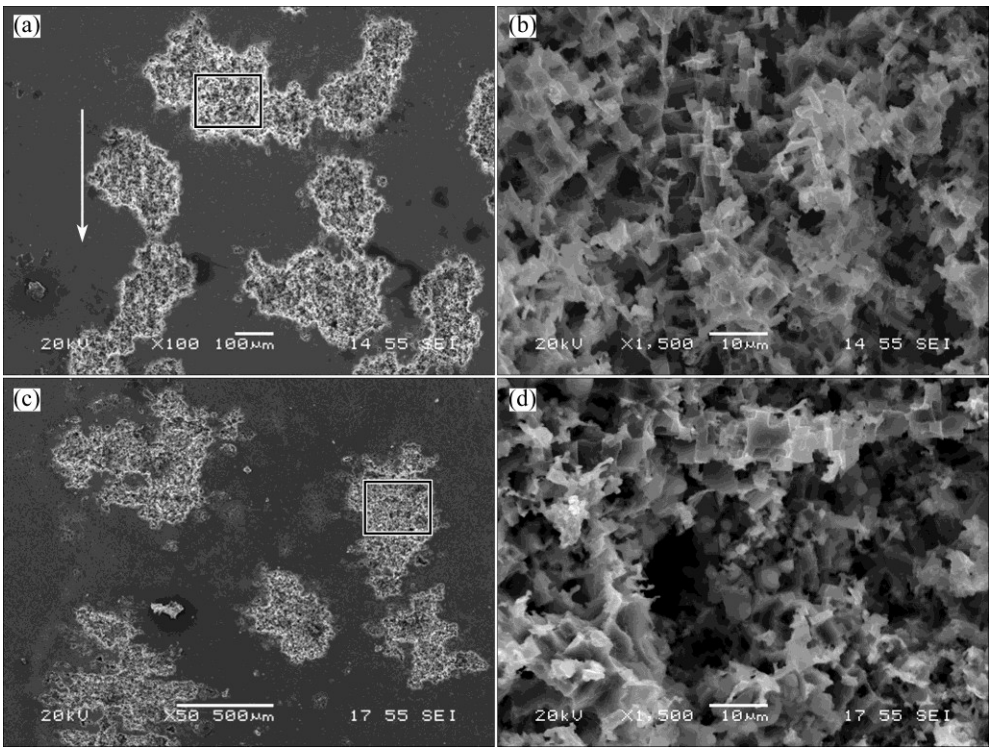

Fig. 7 SEM images of alloy in SHT (a, b) and T3 (c, d) tempers after potentiodynamic polarization from −100 to 500 mV (OCP): (a, c) Alloy surface showing corrosion pits; (b, d) Framed areas in (a) and (c) at increased magnification, respectively

AA2099 alloys in SHT and T3 conditions. At increased magnification (Fig. 8(b)), typical crystallographic corrosion morphology was evident. The relatively well defined facets in Fig. 8(b) compared with Figs. 7(b) and (d) suggest that alloying elements in the alloy influenced the process of crystallographic corrosion. In the regions away from the main pits, initiation of crystallographic corrosion pits was also revealed, as shown in Figs. 8(c) and (d). The propagation path of the crystallographic corrosion was suggested by Fig. 8(d), where several small pits were revealed at the bottom of a relatively large pit (as indicated by the arrow).

In order to show the early stages of localized corrosion, the alloy in T8 was also potentiodynamically polarized to relatively low voltages. Figure 9 shows scanning electron micrographs of the alloy in T8 condition after polarization to 200 mV (OCP), revealing a localized corrosion site in its early stage (Fig. 9(a)). It is evident that the localized corrosion propagated preferentially along the extrusion/stretching direction. Figure 9(b) shows the framed region in Fig. 9(a) at increased magnification, clearly revealing the corroded volume in relatively dark appearance and the intact alloy in relatively bright/gray appearance. Scrutiny of Fig. 9(b) reveals two sets of narrow, parallel, dark lines of corroded volume in the attacked grains, which were orientated approximately 35° to the extrusion/stretching direction and orientated approximately 70° to each other. According to geometry of the narrow, parallel, dark lines, it is believed that they were associated with slip

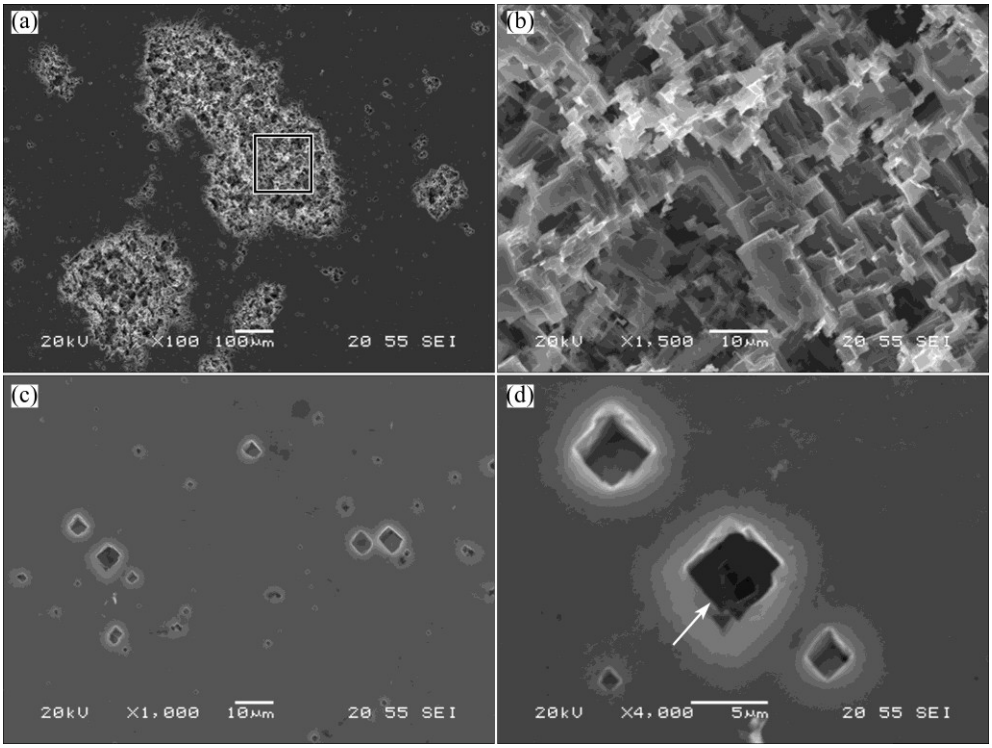

Fig. 8 SEM images of pure aluminum after potentiodynamic polarization from −100 to 500 mV (OCP)

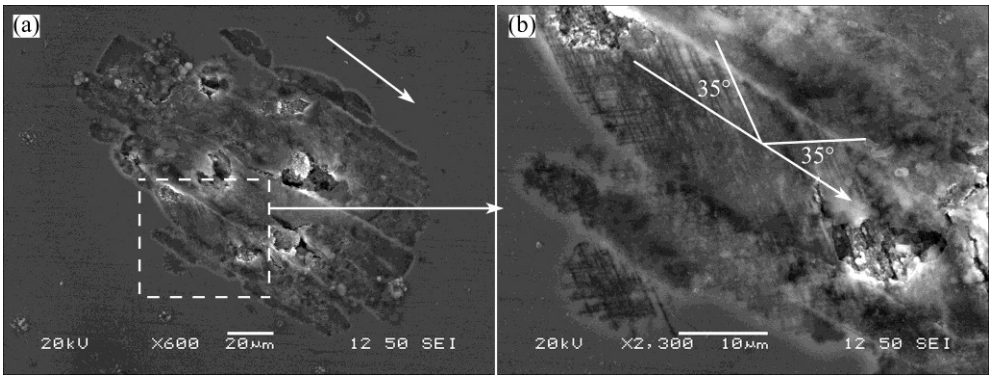

Fig. 9 SEM images of alloy in T8 after potentiodynamic polarization from −100 to 200 mV (OCP) (Arrow in (a) indicates extrusion/stretching direction)

bands [26,27]. The two sets narrow, parallel, dark lines corresponded to slip bands formed in two individual slip systems in the grain.

3.3 Immersion testing

Immersion testing was employed to compare, visually and directly, the resistance of the alloy of different tempers to SLC. The evolution of hydrogen gas and development of corrosion product rings were used as indicators of SLC [19,21]. After immersion in the 3.5% NaCl solution for 5 h, typical SLC was observed on the alloy in T8 condition but little evidence of SLC was detected on the SHT, T3 and T6 specimens, suggesting that the alloy in T8 condition was more susceptible to SLC than the alloy in other conditions. Figure 10 compares the surface morphologies of the alloys in T8 and T6 conditions after the immersion test. It is noted that the SLC sites are elongated in the extrusion/ stretching direction.

4 Discussion

The electrochemistry measurements (Fig. 3) indicate that the corrosion potentials of the T6 and T8 specimens were shifted to more negative direction compared with those of the SHT and T3 specimens. This agrees with the work of PROTON et al [14], who studied the influence of artificial aging on the corrosion behavior of a 2050 Al−Cu−Li alloy and found that different corrosion behaviors of the alloy in different stages of artificial aging were associated with the distribution of the T_1 phase. The T_1 phase only appeared at the grain

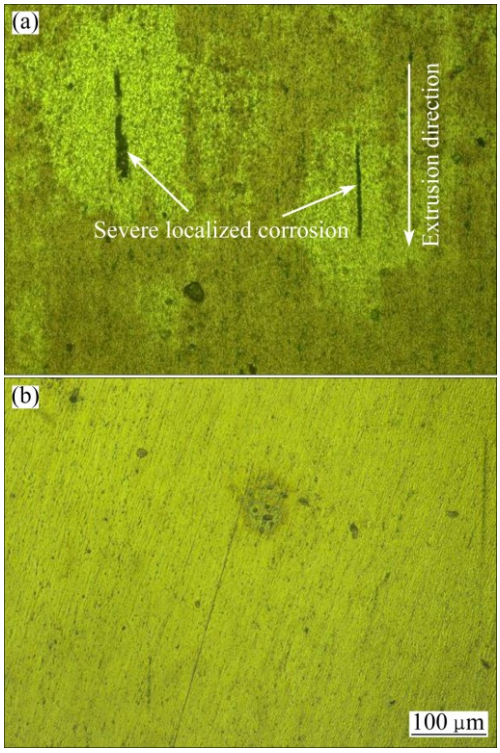

Fig. 10 Optical micrographs of alloy after immersion in 3.5% NaCl solution at ambient temperature for 5 h: (a) T8 condition; (b) T6 condition

boundaries in the as-rolled alloy; while for the heat-treated alloy, it was found that the volume fraction of the T_1 phase in grain interiors increased with the increase of aging time. Consequently, the as-rolled alloy and the alloy aged for short time were susceptible to intergranular corrosion but the alloy aged for more than 9 h was susceptible to intragranular corrosion.

Interestingly, it was revealed in Fig. 4 that the surface area fraction of corrosion pits on the T8 specimen was smaller than other specimens. Since the current densities of the alloy in different tempers were comparable at high potentials (Fig. 3), the reduced surface area fraction of corrosion pits on the T8 specimen means more severe corrosion beneath the alloy surface, i.e. higher susceptibility to SLC. The higher susceptibility of the T8 specimen to SLC was also confirmed by the immersion testing (Fig. 10). Such phenomenon has been rarely reported before and, therefore, deserves further discussion.

It is known that cold working can increase the dislocation density in metals. For face-centered cubic metal such as aluminum, the population density of dislocation in individual grains is highly dependent on their orientation with respect to the cold working direction, when the metal is subjected to relatively low or intermediate strain [28−30]. This is because grains with different orientations have different numbers and types of active slip systems and consequently are subjected to different extents of deformation. Thus, more dislocations will be introduced in the grains which have experienced more plastic deformation relative to other grains. In this work, the SHT specimen was cold-stretched to 3% elongation, which corresponds to relatively low strain. Therefore, it is expected that grains of different orientations in the T3 specimen would experience different extents of plastic deformation and, therefore, the dislocation densities in individual grains would be different [19−21]. Consequently, microstructural localization was generated in the alloy after cold working. Such microstructural localization could influence subsequent artificial aging. It has been widely accepted that T_1 phase preferentially nucleates on crystallographic imperfections such as grain boundaries and dislocations [31,32]. Therefore, when the cold worked alloy was subjected to artificial aging, increased volume fraction of T_1 precipitates would be formed in grains with relatively high dislocation density.

The non-uniform distribution of T_1 precipitates had a significant impact on localized corrosion susceptibility. The corrosion potential of T_1 phase in 3.5% NaCl solution is −1096 mV (vs SCE) [33], which is 346 mV more negative than that of aluminum (−750 mV (vs SCE) [34]). Due to the high electrochemical activity of T_1 phase, localized corrosion was promoted in the regions containing relatively high volume fraction of T_1 phase. This is supported by the revelation of the traces of corroded slip bands, appearing as narrow, parallel, dark lines, in the T8 specimen after potentiodynamic polarization (Fig. 9(b)). Due to dislocation multiplication/pileup, the population density of dislocations on the easy slip planes increased as the deformation proceeded. A dense dislocation band was formed in parallel, easy slip planes. During the artificial aging, the formation of the T_1 phase at dislocations was promoted, resulting in bands with relatively high population density of T_1 phase. Since the T_1 phase is electrochemically more active than the grain matrix, localized corrosion propagated at the bands with dense T_1 phase precipitates, resulting in the selectively corroded bands.

Apart from the localized corrosion susceptibility, it was found that the propagation mechanism of localized corrosion also depended on thermomechanical treatments. As revealed in Figs. 7 and 8, the corrosion morphology of the alloy in SHT and T3 conditions was similar to that of pure aluminum, i.e., crystallographic corrosion. However, the characteristic of crystallographic corrosion was absent at the corrosion sites in T6 and T8 specimens. This suggests that when alloying elements are accommodated in solid solution, the alloy behaved as the pure aluminum under the testing condition. Since T_1 precipitate is more active than aluminum matrix in the

corrosive environment [14,15,33,34], for the T6 and T8 specimens, corrosion propagation along the crystallographic planes should have been diverted by the active precipitates, preventing the formation of typical crystallographic corrosion morphology. Further, the less well-defined crystallographic corrosion in the SHT and T3 specimens compared with the pure aluminum suggests that alloying elements in solid solution might also influence the corrosion propagation process at the atomic level, although such influence was not as significant as the precipitates.

5 Conclusions

1) The susceptibility of the AA2099 Al−Li alloy to localized corrosion was sensitive to thermomechanical treatments. The alloy of T8 condition showed higher susceptibility to severe localized corrosion than solution heat-treated, T3 and T6 conditions.

2) Severe localized corrosion in the alloy of T8 condition was associated with localized plastic deformation occurring during pre-age cold working and heterogeneous precipitation of T_1 (Al_2CuLi) phase during subsequent artificial aging.

3) The state of alloying elements in the AA2099 Al−Li alloy influenced the mechanism of localized corrosion propagation during potentiodynamic polarization. The alloy in solution heat treated and T3 conditions displayed crystallographic corrosion morphology while the alloy in T6 and T8 conditions exhibited selective attack of grain boundaries and grain interiors.

References

[1] RIOJA R J. Fabrication methods to manufacture isotropic Al−Li alloys and products for space and aerospace applications [J]. Material Science and Engineering A, 1998, 257(1): 100−107.

[2] GURAO N P, ADESOLA A O, ODESHI A G, SZPUNAR J A. On the evolution of heterogeneous microstructure and microtexture in impacted aluminum−lithium alloy [J]. Journal of Alloys Compounds, 2013, 578: 183−187.

[3] GAO C, LUAN Y, YU J C, MA Y. Effect of thermo-mechanical treatment process on microstructure and mechanical properties of 2A97 Al−Li alloy [J]. Transactions of Nonferrous Metals Society of China, 2014, 24(7): 2196−2202.

[4] LIU Bing, PENG Chao-qun, WANG Ri-chu, WANG Xiao-feng, LI Ting-ting. Recent development and prospects for giant plane aluminum alloys [J]. The Chinese Journal of Nonferrous Metals, 2010, 20(9): 1705−1715. (in Chinese)

[5] MA Y, ZHOU X, THOMPSON G E, HASHIMOTO T, THOMSON P, FOWLES M. Distribution of intermetallics in an AA 2099-T8 aluminium alloy extrusion [J]. Materials Chemistry and Physics, 2011, 126(1−2): 46−53.

[6] MARTIN J W. Aluminum−lithium alloys [J]. Annual Review of Materials Science, 1988, 18: 101−119.

[7] LIU J. Advanced aluminium and hybrid aero-structures for future aircraft [J]. Material Science Forum, 2006, 519−521: 1233−1238.

[8] DURSUN T, SOUTIS C. Recent developments in advanced aircraft aluminium alloys [J]. Material and Design, 2014, 56: 862−871.

[9] BUCHHEIT R G, MORAN J P, STONER G E. Localized corrosion behavior of alloy 2090: The role of microstructural heterogeneity [J]. Corrosion, 1990, 46(8): 610−617.

[10] BUCHHEIT R G, MORAN J P, STONER E. Electrochemical behavior of the T_1(Al_2CuLi) intermetallic compound and its role in localized corrosion of Al−2%Li−3%Cu alloys [J]. Corrosion, 1994, 50(2): 120−130.

[11] KERTZ J E, GOUMA P I, BUCHHEIT R G. Localized corrosion susceptibility of Al−Li−Cu−Cu−Mg−Zn alloy AF/C 458 due to interrupted quenching from solutionizing temperatures [J]. Metallurgical and Materials Transactions A: Physical Metallurgy and Materials Science A, 2001, 32: 2561−2573.

[12] ROMIOS M, TIRASCHI R, PARRISH C, BABEL H W, OGREN J R, ES-SAID O S. Design of multistep aging treatments of 2099 (C458) Al−Li−Cu based alloy [J]. Journal of Materials Engineering and Performance, 2005, 14(5): 641−646.

[13] PROTON V, ALEXIS J, ANDRIEU E, DELFOSSE J, LAFONT M C, BLANC C. Characterisation and understanding of the corrosion behaviour of the nugget in a 2050 aluminium alloy friction stir welding joint [J]. Corrosion Science, 2013, 73: 130−142.

[14] PROTON V, ALEXIS J, ANDRIEU E, DELFOSSE J, DESCHAMPS A, DEGEUSER F, LAFONT M C, BLANC C. The influence of artificial ageing on the corrosion behaviour of a 2050 aluminium−copper−lithium alloy [J]. Corrosion Science, 2014, 80: 494−502.

[15] LI J F, ZHENG Z Q, LI S C, CHEN W J, REN W D, ZHAO X S. Simulation study on function mechanism of some precipitates in localized corrosion of Al alloys [J]. Corrosion Science, 2007, 49: 2436−2449.

[16] WARNER T. Recently-developed aluminium solutions for aerospace applications [C]//Material Science Forum. Swizenand: Trans Tech Publications, 2006: 1271−1278.

[17] LI H Y, TANG Y, ZENG Z D, ZHENG F. Exfoliation corrosion of T6- and T8-aged $Al_xCu_yLi_z$ alloy [J]. Transactions of Nonferrous Metals Society of China, 2008, 18(4): 778−783.

[18] PAN Q L, LI Y C, LIANG W J, HE Y B, ZHOU Y C, LU C G, LIU X Y. Influence of pre-deformation on exfoliation corrosion behavior of Al−Cu−Li−Zr alloy containing Sc [J]. J Cent South Univ (Science and Technology), 2008, 39(4): 735−740. (in Chinese)

[19] ZHOU X, LUO C, MA Y, HASHIMOTO T, THOMPSON G E, HUGHES A E, SKELDON P. Grain-stored energy and the propagation of intergranular corrosion in AA2xxx aluminium alloys [J]. Surface and Interface Analysis, 2013, 45(10): 1543−1547.

[20] MA Y, ZHOU X, HUANG W, LIAO Y, CHEN X, ZHANG X, THOMPSON G E. Crystallographic defects induced localized corrosion in AA2099-T8 aluminium alloy [J]. Corrosion Engineering, Science Technology, 2015, 50(6): 420−424.

[21] MA Y, ZHOU X, HUANG W, THOMPSON G E, ZHANG X, LUO C, SUN Z. Localized corrosion in AA2099-T8 aluminum−lithium alloy: The role of intermetallic particles [J]. Materials Chemistry and Physics, 2015, 161(1): 201−210.

[22] BAUMGÄRTNER M, KAESCHE H. Aluminum pitting in chloride solutions: Morphology and pit growth kinetics [J]. Corrosion Science, 1990, 31: 231−236.

[23] ABALLE A, BETHENCOURT M, BOTANA F J, CANO M J, MARCOS M. Localized alkaline corrosion of alloy AA5083 in neutral 3.5% NaCl solution [J]. Corrosion Science, 2001, 43: 1657−1674.

[24] AMBAT R, DAVENPORT A J, SCAMANS G M, AFSETH A. Effect of iron-containing intermetallic particles on the corrosion behaviour of aluminium [J]. Corrosion Science, 2006, 48: 3455−3471.

[25] ZAID B, SAIDI D, BENZAID A, HADJI S. Effects of pH and chloride concentration on pitting corrosion of AA6061 aluminum alloy [J]. Corrosion Science, 2008, 50: 1841−1847.
[26] LEE E H, YOO M H, BYUN T S, HUNN J D, FARRELL K, MANSUR L K. On the origin of deformation microstructures in austenitic stainless steel: Part II. Mechanisms [J]. Acta Materialia, 2001, 49(16): 3277−3287.
[27] SMITH W F, HASHEMI J. Foundation of materials science and engineering [M]. 4th ed. Beijing: China Machine Press, 2006.
[28] HANSEN N, JENSEN D J. Development of microstructure in FCC metals during cold work [J]. Philosophical Transactions of the Royal Society of London (Series A), 1999, 357(1756): 1447−1469.
[29] LIU Q, JENSEN D J, HANSEN N. Effect of grain orientation on deformation structure in polycrystalline aluminium [J]. Acta Materialia, 1998, 46(16): 5819−5838.
[30] GODFREY A, HANSEN N, JENSEN D J. Microstructural-based measurement of local stored energy variations in deformed metals [J]. Metallurgical and Materials Transactions A: Physical Metallurgy and Materials Science A, 2007, 38(13): 2329−2339.
[31] GABLE B M, ZHU A W, CSONTOS A A, STARKE E A Jr. The role of plastic deformation on the competitive microstructural evolution and mechanical properties of a novel Al−Li−Cu−X alloy [J]. Journal of Light Metals, 2001, 1(1): 1−14.
[32] YOSHIMURA R, KONNO T J, ABE E, HIRAGA K. Transmission electron microscopy study of the evolution of precipitates in aged Al−Li−Cu alloys: The θ' and T_1 phases [J]. Acta Materialia, 2003, 51(14): 4251−4266.
[33] BUCHHEIT R G. A Compilation of corrosion potentials reported for intermetallic phases in aluminum alloys [J]. Journal of the Electrochemical Society, 1995, 142(11): 3994−3996.
[34] VARGEL C, JACQUES M, SCHMIDT M P. Corrosion of aluminum [M]. Oxford: Elsevier, 2004.

热机械加工对 AA2099 铝锂合金局部腐蚀敏感性及其扩展机理的影响

麻彦龙[1]，Xiao-rong ZHOU[2]，孟晓敏[1]，黄伟九[1]，廖 益[3]，
陈小丽[1]，易雅楠[1]，Xin-xin ZHANG[2], G. E. THOMPSON[2]

1. 重庆理工大学 材料科学与工程学院，重庆 400054；
2. Corrosion and Protection Centre, School of Materials, University of Manchester, Manchester M13 9PL, UK；
3. 重庆教育学院，重庆 400067

摘 要：为了突出特定显微组织组成对 AA2099 铝锂合金严重局部腐蚀的影响，对比研究了固溶、预冷变形及人工时效状态下 AA2099 合金的腐蚀行为。通过浸泡和动电位极化在合金表面引入局部腐蚀；采用扫描电子显微镜和透射电子显微镜表征合金的显微组织和腐蚀形貌。研究表明：该合金的严重局部腐蚀敏感性与其热机械加工过程密切相关，且合金元素的存在方式影响腐蚀的扩展机理。T8 状态合金的严重局部腐蚀敏感性比其他状态合金更高；当进行动电位极化时，固溶和 T3 状态合金表现为晶体学腐蚀特征而 T6 和 T8 状态合金表现为局部区域晶粒和晶界的择优腐蚀。

关键词：铝锂合金；腐蚀；点蚀；极化；热处理

(Edited by Xiang-qun LI)